
Orthogonalization Principle for Dynamic Visual Servoing of Constrained Robot Manipulators

Vicente Parra-Vega and Emmanuel Dean-Leon

Mechatronics Division - Research Center for Advanced Studies (CINVESTAV)
IPN Av. 2508, San Pedro Zactenco, Mexico City, 07300, Mexico.
Email: (vparra, edean)@cinvestav.mx

Summary. A monocular visual servoing scheme for constrained robots is considered in this chapter. Inspired by the Orthogonalization Principle (OP) introduced by Suguru Arimoto in the context of robot force control, a Visual Orthogonalization Principle (VOP) is proposed and a novel control scheme for adaptive image-based visual servoing is presented. The scheme guarantees a global *exponential convergence* for the image-based position-velocity and contact forces even when the robot parameters are considered unknown. The stability of the new control scheme is tested under experiments. The experimental results comply to the theoretical considerations.

1 Introduction

Since the publication of the work [1] in 1977 the problem of robot force control represented a tremendous challenge in the robotics and control community for over 15 years [2], [3], [4]. Many control schemes were proposed to deal with the problem on how to exert force by a robot manipulator over a rigid surface while simultaneously moving its end-effector along this surface. The main difficulty in this problem stemmed from the fact that when the robot is in contact to a rigid surface, modeled by an implicit equation, it is geometrically constrained. This can be modeled by the algebraic differential equations (DAE). Recognizing this fact, a new controller based on the DAE formulation was introduced in [5]. There, it was proposed to project the n degrees of freedom robot dynamics into two orthogonal subspaces complements, one related to the force signals and the other related to the position signals, to derive a global, asymptotically stable simultaneous force-position controller. However, this approach results in a computationally expensive control scheme.

It was not until 1992 that a physically-based principle was introduced [6] to formally solve this problem in the powerful settings of the passivity-based control theory. The principle is based the fundamental interpretation, made

by Suguru Arimoto, of what physically happens when the end-effector of a rigid body system with n degrees of freedom comes in contact to, and establish motion over, a rigid surface. This principle was coined as the ‘‘Orthogonalization Principle’’ (OP) and applied to the control of robot manipulators constrained by a rigid surface modeled by an implicit equation. In [6], the OP was introduced to produce a simple nominal reference based on two orthogonal complements without projecting and decomposing the robot dynamics. The result was a local asymptotically stable force-position controller. Later on, this basic principle allowed the synthesis of motion control for such complex systems as cooperating robot arms [7] and multi-fingered robotic hands [8]. In this chapter, an extension of the OP is introduced to tackle the problem of the passivity-based monocular adaptive visual servoing for constrained robot manipulators. It is shown that the extended OP produces second order sliding modes, guaranteeing a global exponential tracking.

2 The Orthogonalization Principle: Robot Force Control

2.1 Constrained robot dynamics

Consider a robot whose gripper maintains a stable contact to an infinitely rigid surface. According to [6], this system is modeled by the following nonlinear differential algebraic equations

$$H(q)\ddot{q} + C(q, \dot{q})\dot{q} + g(q) = \tau + J_{\varphi+}^T(q)\lambda \quad (1)$$

$$\varphi(q) = 0 \quad (2)$$

where the generalized joint position $q \in \mathfrak{R}^n$ and the joint velocity $\dot{q} \in \mathfrak{R}^n$. In (1), matrix $H(q) \in \mathfrak{R}^{n \times n}$ stands for the robot inertial matrix; $C(q, \dot{q})\dot{q} \in \mathfrak{R}^n$ stands for the vector of centripetal and Coriolis torques; $g(q) \in \mathfrak{R}^n$ is the vector of gravitational torques; $J_{\varphi+}(q) = \frac{J_{\varphi}(q)}{J_{\varphi}(q)J_{\varphi}^T(q)} \in \mathfrak{R}^{n \times m}$ is the constrained normalized Jacobian of the kinematic constraint $\varphi(q) = 0$ (rigid surface with continuous gradient); $\lambda \in \mathfrak{R}^m$ is the constrained Lagrangian multiplier for m contact points (magnitude of the contact force); $\varphi(q) = 0 \in \mathfrak{R}^m$ models the surface (for m independent contact points), and finally $\tau \in \mathfrak{R}^n$ stands for the vector of the joint torques.

2.2 The Orthogonalization Principle

According to the forward kinematic mapping $X = f(q) \in \mathfrak{R}^n$. Since $\varphi(q) = g(X) \equiv 0$, we have

$$\begin{aligned}
 \varphi(q) = 0 &\rightarrow \frac{d}{dt}\varphi(q) = \frac{\partial g(X)}{\partial X} \frac{\partial X(f(q))}{\partial q} \frac{dq}{dt} \equiv 0 \\
 \implies \frac{d}{dt}\varphi(q) &= J_g(x) J_x(q) \dot{q} \\
 &= J_\varphi(q) \dot{q} \equiv 0
 \end{aligned} \tag{3}$$

This means that $J_\varphi(q)$ is orthogonal to \dot{q} in the joint space. Thus, \dot{q} belongs to the kernel of $J_\varphi(q)$. However, it is well known from the classical mechanics that the vector of the generalized velocities lies in the tangent space at the contact point. Therefore, $\dot{q} = Q\dot{q}$, where $Q \in \mathbb{R}^{n \times n}$ stands for the generator of the null space of $J_\varphi(q)$, with $J_\varphi(q)$ being orthogonal to Q . In words, the OP states that \dot{q} can be decomposed of the direct summation of two components, one in the velocity subspace Q and the other in the force subspace $J_\varphi(q)$. The nominal reference for \dot{q} can be constructed similarly. Therefore, a unique orthogonalized velocity joint error signal can be introduced to build a unique open loop error dynamics depending on both the velocity and force error signals. This is the key idea of the seminal paper [6]. Using the OP in the physical interpretation of Arimoto [6], one can build a unique nominal reference in terms of the two orthogonal errors and avoid decomposing the full nonlinear robot dynamics as proposed in [5].

2.3 Passivity of Constrained Robot Dynamics

The integral of the dot product of \dot{q} and τ yields

$$\int_{t_0}^{t_f} \dot{q}^T \tau = E(t_f) - E(t_0) - \underbrace{\dot{q}^T J_{\varphi+}^T(q) \lambda}_{\text{zero}} \leq -E(t_0)$$

where $E(t)$ is the total energy of the robot. Note that the antisymmetry of $[\dot{H}(q) - (C(q, \dot{q}) + C(q, \dot{q})^T)]$ is used in the derivation of this equation. The passivity of the robot dynamics is established then from the joint velocity input \dot{q} to the torque output τ ¹. Since in the force control the objective is the convergence of the position/velocity tracking errors simultaneously with the force tracking error, a unique error signal at the velocity level must be established to conform to the passivity inequality in the closed-loop control. This unique error signal is introduced [6] via the so-called nominal reference \dot{q}_r based on the OP:

$$\dot{q}_r = \dot{q}_v + \dot{q}_f \equiv Q\dot{q}_{ev} + J_\varphi^T \dot{q}_{ef} \tag{4}$$

Equation (4) depends on the orthogonal nominal references for the velocity \dot{q}_v and force \dot{q}_f . Since $\dot{q} = Q\dot{q}$, the extended error surface can be defined follows

$$S_q = \dot{q} - \dot{q}_r \equiv Q(\dot{q} - \dot{q}_{ev}) - J_\varphi^T \dot{q}_{ef} \tag{5}$$

¹ Notice that if viscous friction exists, then the dissipativity is established.

To design a passivity-based controller, the linearity of the left hand side of the robot dynamics in a set of its physical parameters can be used to define:

$$H(q)\ddot{q}_r + C(q, \dot{q})\dot{q}_r + g(q) = Y_r\Theta \quad (6)$$

Here, $Y_r = Y_r(q, \dot{q}, \ddot{q}_r) \in \mathbb{R}^{n \times p}$ is the dynamic regressor matrix, and $\Theta \in \mathbb{R}^p$ stands for the unknown (but constant) vector of the robot parameters. Adding and subtracting (6) to (1) produces the open loop error equation

$$H(q)\dot{S}_q = -C(q, \dot{q})S_q + \tau + J_{\varphi+}^T(q)\lambda - Y_r\Theta$$

Now, if

$$\tau = -K_d S_q + Y_r\Theta - J_{\varphi+}^T(\lambda_d - \eta\Delta F) \quad (7)$$

where $\Delta F = \int_{t_0}^{t_f} (\lambda(\sigma) - \lambda_d(\sigma))d\sigma$, $\lambda_d(t)$ is the desired magnitude of the contact force, K_d is a symmetric positive definite 2×2 feedback gain, and $\eta > 0$, the simultaneous local asymptotic convergence of $\lambda \rightarrow \lambda_d$ and $\dot{q} \rightarrow \dot{q}_{ev}$ is assured. If $\dot{q}_{ev} = \dot{q}_d - \Omega(q - q_d)$ for $\Omega \in \mathbb{R}_+^{2 \times 2}$, then $q \rightarrow q_d$, where q_d stands for the desired motion of the end-effector on the surface [6].

To extend the previous result to the visually driven force control one needs to address two problems. The first one is how to redesign (4) in terms of image coordinates, and the second one is how to produce a visual-based control law (7) to guarantee the simultaneous convergence of the contact force error and the visual coordinate errors in the presence of the robot parametric uncertainties. To this end, we introduce the Visual Orthogonalization Principle (VOP).

3 The Visual Force Control Problem

Similar to the standard force control problem, the OP naturally arises in visual servoing of constrained robot manipulators; the joint space orthogonalization is preserved since the video camera does not introduce any additional dynamics. The problem now is how to synthesize the joint torque input in terms of the desired visual trajectories and guarantee that the contact force error and the visual position error converge simultaneously. This is a very important problem in modern applications, wherein non-invasive sensors, like CCD cameras, are used to guide the system under human surveillance and supervision. In this case, the robot moves along the surface and the camera captures its motion by the optical flow. To solve the control problem at hand, the OP has to be reformulated in the context of the image-based visual coordinates to incorporate visual errors to the nominal reference. This gives rise to the VOP. Note that this type of robot control tasks involves significant difficulties. It stands as a robot control paradigm that surpasses traditional schemes in robot control and sensor fusion, thus requiring new theoretical frameworks. In our problem, the VOP fuses generalized sensors (measurement of encoder,

tachometer, moment and force), and non-generalized sensors (CCD camera) through the nominal reference \dot{q}_r . To continue the explanation, it is necessary to briefly review the dynamic visual servoing.

3.1 Visual Servoing

Visual servoing is an ill-posed control scheme because measurements from the camera do not deliver directly the state of the system, and thus cannot be modified directly by the control input to the robot. Besides, the optical flow (velocity of the visual landmarks) is not orthogonal to the joint torque input. To make clear the choice between the position-based and image-based visual servoings, the following features of these techniques [9] should be noted:

1. **Position-based servoing:** The image coordinates are transformed into generalized coordinates to compute the control laws. This approach is prone to errors due to this transformation and is computationally difficult.
2. **Image-based servoing:** The target to be tracked is captured and the computed error in the image plane is obtained. Then, the joint control input is synthesized to ensure asymptotic behavior of the visual error. This approach is robust to the camera calibration since the tracking error remains in the visual coordinates.

The image-based visual servoing is more practical because, in addition to the arguments pointed in item 2, the user can input the desired position directly in the image task space, i.e., directly from the image she/he sees. The research on visual servoing started with the pioneering work [10] and so far several authors extended the scope [11]~[18]. In 1993, the authors of [11] proposed a model and an adaptive control scheme for an eye-in-hand system where the depth of each feature was estimated at each sampling time. In [12], the authors introduced a new technique called a visual compliance that was achieved by a hybrid vision/position control structure. Some authors included the nonlinear robot dynamics in the control design [14]~[17]. Some of them modeled the vision system by a simple rotation matrix [14], others proposed a variety of techniques for the off-line camera calibration [13], and only a few approaches were aimed at the more important problem of the on-line calibration under the closed loop control. Specifically, for a *fixed camera* configuration, the authors of [15] considered a more representative model of the camera-robot system to design a control law that compensates for unknown intrinsic camera parameters but requires the exact knowledge of the camera orientation.

Later, the authors of [16] presented a redesigned control law that also takes into account uncertainties in the camera orientation. The control law features the local asymptotic stability but requires the perfect knowledge of the robot gravitational terms, and the error of the estimation of camera orientation is restricted to $(-90^\circ, 90^\circ)$. Further developments were presented in

[13], wherein a position tracking control scheme with an on-line adaptive calibration of the camera that guaranteed the global asymptotic position tracking was presented. Nevertheless, this approach requires the knowledge of the robot dynamics and the desired trajectories need to be persistently excited. In [17], the authors designed an adaptive camera calibration control law that compensates for the uncertain camera parameters and the entire robot-camera system, achieving the global *asymptotic* position tracking. Recently, a robust and continuous joint PID-like controller was introduced in [18]. This scheme guarantees the exponential convergence of the image-based tracking errors, in spite of the lack of the knowledge of the camera and robot parameters. In comparison to the approaches considered above, it does not presents limitations on the camera orientation.

Despite of the availability of various approaches considered in this section, none of them fuses the force information for the image-based tracking of the constrained robot systems. The robot control problem is still elusive, though [19] lights the path for the passivity-based dynamic tracking in visual servoing schemes. However, it fails when the camera angle is close to π [19].

3.2 Fusing Visual and Joint Signals

When only the sensors associated with the generalized coordinates are involved in robot force control, the OP unobtrusively provides a harmonious unique error signal, combining the position and contact force errors. However, when the robot tasks involve also non-generalized sensors², the control law must deal with the multisensor fusion of the force and joint encoders signals along with the visual information. Therefore, in order to implement a sensor fusion-based controller, a careful and judicious analysis of the robot nonlinear dynamics, sensors behavior, and the contact tasks is required. To continue, let us review briefly some visual-based force servoing schemes.

3.3 Visual Force Servoing

The reference [21] focuses on the sensor fusion of the force and visual landmarks. The authors of [22] study a visual contour tracking in a structured environment. In [23], the authors present an adaptive robot controller to realize contact tasks in an unknown environment. In [23] it is assumed that the movement of the camera-manipulator system is slow and the mapping from the joint space to the image space is constant, which severely limits the system performance. Along similar developments, the paper [20] presents a computed torque scheme for an uncalibrated environment, which requires the exact knowledge of the robot dynamics and relies upon a very complex control law. The control laws in [23] and [20] require complex computations and do not fully solve the control problem posed above.

² For example a CCD camera. The non-generalized sensors do not directly measure the state variables of the robot dynamic equations.

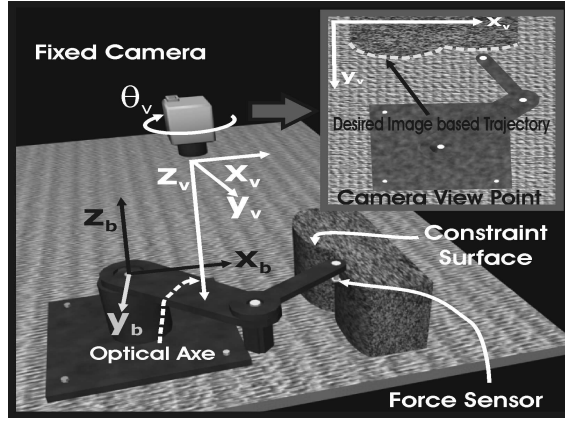


Fig. 1. Visual servoing of the contact task.

4 Dynamics of the Visually Driven Constrained Robot

Here, a monocular visual servoing scheme is presented³. In order to design a proper *nominal reference* for the joint velocities \dot{q}_r , the direct and inverse robot kinematics, based on the static pin hole, with thin lens without aberration camera model [9], is used. Let the direct kinematics of the robot be

$$x_b = f(q) \quad (8)$$

where $x_b \in \mathbb{R}^2$ represents the 2D position of robot end-effector in the robot work space and $f(\cdot) : \mathbb{R}^2 \rightarrow \mathbb{R}^2$. The differential kinematics of the robot manipulator is defined as follows

$$\dot{x}_b = J(q)\dot{q} \quad (9)$$

It relates the Cartesian velocities $\dot{x}_b \in \mathbb{R}^2$ to the joint space velocities $\dot{q} \in \mathbb{R}^2$. The visual position $x_v = [u, v]^T \in \mathbb{R}^2$ of the robot end-effector in the image (screen) space⁴ is given as follows [9]

$$x_v = \alpha h(z)R(\theta_v)x_b + \beta \quad (10)$$

where $\alpha = \text{diag}[\alpha_u, \alpha_v] \in \mathbb{R}_+^{2 \times 2}$ is the scale factor; $h(z) = \frac{\xi}{\xi - z} < 0$, $z > \xi$. Here, ξ stands for the focal distance, and $R(\theta_v) \in SO(2)$ is the upper left 2×2

³ Explicitly, this means that the 2D case is considered and the image plane is parallel to the 2D work plane of the nonlinear DAE robot. Notice, however, that the extension to the 3D case, though straightforward, requires a stereo camera model with additional considerations for the (pseudo)inverse of the differential kinematic mapping.

⁴ The subscript v of x_v denotes *visual* from the *visual space* notation.

matrix of $R_3(\theta_v) \in SO(3)$; $\beta \in \mathfrak{R}_+^2$, depends on the intrinsic and extrinsic parameters⁵ of the camera. The differential kinematic model of the camera is defined as follows

$$\dot{x}_v = \alpha h(z) R(\theta_v) \dot{x}_b \quad (11)$$

where $\dot{x}_v \in \mathfrak{R}^2$ determines the visual robot end-effector velocity, i.e. the *visual flow*. Notice that the transformation $\alpha h(z) R(\theta)$ is constant and it maps statically the robot *Cartesian velocities* \dot{x}_b into the *visual flow* \dot{x}_v . By using (9), equation (11) becomes

$$\dot{x}_v = \alpha h(z) R(\theta_v) J(q) \dot{q} \quad (12)$$

It relates the *visual flow* \dot{x}_v to the *joint velocity vector* \dot{q} . Thus, in terms of the visual velocities⁶ the inverse differential kinematics (12) becomes

$$\dot{q} = J_{Rinv} \dot{x}_v \quad (13)$$

where $J_{Rinv} = J(q)^{-1} R(\theta)^{-1} h(z)^{-1} \alpha^{-1}$. This relation is useful in designing the nominal reference for the joint velocities \dot{q}_r .

4.1 Visual Orthogonalization Principle (VOP)

Since the robot end-effector is in contact to the constrain surface, $\varphi(q) = 0 \forall t$ and the OP explains the implications of $\frac{d}{dt} \varphi(q) = 0$. Therefore, using (13) we obtain

$$J_\varphi(q) \dot{q} = \dot{q} \equiv J_\varphi J_{Rinv} \dot{x}_v \doteq 0$$

This means that $J_\varphi(q)$ is orthogonal to the optical flow \dot{x}_v mapped into the joint space. Clearly, there exists an orthogonal projection Q of $J_\varphi(q)$ which spans the tangent space at the contact point between the end-effector and the surface $\varphi(q) = 0$. In other words, (13) and $\dot{q} = Q\dot{q}$ leads to

$$\dot{q} = Q J_{Rinv} \dot{x}_v \quad (14)$$

From (4) and (14), the nominal reference for VOP becomes

$$\dot{q}_r = Q J_{Rinv} \dot{x}_r + \dot{q}_f \quad (15)$$

Finally

$$\dot{q}_r = Q J_{Rinv} \dot{x}_r + \Gamma_{F_2} J_\varphi^T(q) \dot{q}_{rf} \quad (16)$$

where $\Gamma_{F_2} > 0$ is a 2×2 feedback gain. Let the *nominal visual reference* for the velocities be

⁵ The focal distance, the depth of the field, the translation of the camera center to the image center, and the distance between the optical axis and the robot base.

⁶ The entries of $J_{Rinv} \in \mathfrak{R}^{2 \times 2}$ are functions of the robot and camera parameters.

$$\dot{x}_r = \dot{x}_{vd} - \Psi \Delta x_v + S_{vd} - \Gamma_{v_1} \int_{t_0}^t S_{v\delta}(\zeta) d\zeta - \Gamma_{v_2} \int_{t_0}^t \text{sign}[S_{v\delta}(\zeta)] d\zeta \quad (17)$$

where \dot{x}_{vd} stands for the desired visual velocity trajectory, and $\Delta x_v = x_v - x_{vd}$ is the visual position tracking error, $\Psi > 0$ a positive definite $n \times n$ feedback gain, and $\Gamma_{v_i} = \Gamma_{v_i}^T \in \mathfrak{R}_+^{n \times n}$, $i = 1, 2$. Let the *visual error surface* be

$$S_{v\delta} = \underbrace{(\Delta \dot{x}_v + \Psi \Delta x_v)}_{S_v} - \underbrace{S_v(t_0) e^{-\kappa_v t}}_{S_{vd}} \quad (18)$$

where $\Delta \dot{x}_v = \dot{x}_v - \dot{x}_{vd}$ defines the visual velocity tracking error, $\kappa_v > 0$. Now, consider the following *nominal force reference*

$$\dot{q}_{rf} = \Delta F - S_{Fd} + \Gamma_{F_1} \int_{t_0}^t S_{F\delta}(\zeta) d\zeta + \Gamma_{F_2} \int_{t_0}^t \text{sign}[S_{F\delta}(\zeta)] d\zeta \quad (19)$$

for the *force error surface*

$$S_{F\delta} = \underbrace{\Delta F}_{S_F} - \underbrace{S_F(t_0) e^{-\kappa_F t}}_{S_{Fd}} \quad (20)$$

where

$$\Delta F = \int_{t_0}^t \Delta \lambda(\zeta) d\zeta, \quad \Delta \lambda = \lambda - \lambda_d,$$

$\Delta \lambda$ is the force tracking error and λ_d is the desired contact force; $\kappa_F > 0$, and $\Gamma_{F_i} = \Gamma_{F_i}^T \in \mathfrak{R}_+^{m \times m}$, $i = 1, 2$. Using equations (16), (17), (19) and (14), we obtain the following representation for the *joint error surface* $S_q \dot{q} - \dot{q}_r$

$$\begin{aligned} S_q &= Q J_{Rinv}(\dot{x}_v - \dot{x}_r) - \Gamma_{F_2} J_\varphi^T(q) \dot{q}_{rf} \\ &= Q J_{Rinv} S_{vv} - \Gamma_{F_2} J_\varphi^T(q) S_{vF} \end{aligned} \quad (21)$$

where

$$S_{vv} = S_{v\delta} + \Gamma_{v_1} \int_{t_0}^t S_{v\delta}(\zeta) d\zeta + \Gamma_{v_2} \int_{t_0}^t \text{sign}[S_{v\delta}(\zeta)] d\zeta \quad (22)$$

$$S_{vF} = S_{F\delta} + \Gamma_{F_1} \int_{t_0}^t S_{F\delta}(\zeta) d\zeta + \Gamma_{F_2} \int_{t_0}^t \text{sign}[S_{F\delta}(\zeta)] d\zeta \quad (23)$$

S_{vv} stands for the *extended visual manifold*, and S_{vF} stands for the *extended force manifold*.

Remark 1. Notice that S_q is composed of two orthogonal complements. The first, $Q J_{Rinv} S_{vv}$, depends on the image coordinate errors, and the second, $\Gamma_{F_2} J_\varphi^T(q) S_{vF}$, depends on the integral of the contact force errors. Thus, the tracking errors $(\Delta x_v, \Delta \dot{x}_v)$ and ΔF can be controlled independently within a single control loop.

4.2 Global Decomposition of Joint Space

Consider the following partition of the joint space q [5], [24]

$$q = [q_1, q_2]^T \quad (24)$$

where $q_1 \in \mathfrak{R}^m$, and $q_2 \in \mathfrak{R}^{n-m}$. Since the constraint $\varphi(q) \in \mathfrak{R}^m$, there are m dependent states which are defined in (24) as q_1 . This partition is not arbitrary. Thus, to identify q_1 the Jacobian of the restriction $J_\varphi(q)$ and the Gauss decomposition are used in order to define a non-singular matrix $m \times m$. The generalized coordinates defined by the choice of this matrix are indeed q_1 [25]. According to the implicit function theorem, there exist, locally, an open group $O \in \mathfrak{R}^{n-m}$ and a function $\Omega : \mathfrak{R}^{n-m} \rightarrow \mathfrak{R}^m$ such that

$$q_1 = \Omega(q_2) \quad (25)$$

Then, $\varphi(q) = \varphi(\Omega(q_2), q_2) = 0 \forall q_2 \in O$. Using the time derivative of (2) and its partitioning (24), we obtain

$$J_\varphi(q) \dot{q} = [J_{\varphi_1}(q) \dot{q}_1 + J_{\varphi_2}(q) \dot{q}_2] \equiv 0 \quad (26)$$

where $J_{\varphi_1}(q) \dot{q}_1 \in \mathfrak{R}^m$ and $J_{\varphi_2}(q) \dot{q}_2 \in \mathfrak{R}^m$. Solving (26) for \dot{q}_1 defines

$$\dot{q}_1 = \Omega_{q_2} \dot{q}_2, \quad \text{where} \quad \Omega_{q_2} = -[J_{\varphi_1}(q)]^{-1} J_{\varphi_2}(q)$$

for $\Omega_{q_2} : \mathfrak{R}^{n-m} \rightarrow \mathfrak{R}^m$. Then, joint velocities are built upon the independent coordinates

$$\dot{q} = Q \dot{q}_2, \quad \text{where} \quad Q = [\Omega_{q_2}, I_{n-m}]^T \quad (27)$$

and $Q \in \mathfrak{R}^{n \times (n-m)}$ is a full column matrix of rank $(n-m)$. Then, Q is well posed, $\text{rank}(\varphi(q)) = m$ and $(J_{\varphi_1}(q))^{-1}$ exists in the finite workspace of (1). Notice again that Q spans the tangent plane at the contact point, and, therefore, $J_\varphi(q)$ and Q are the orthogonal complements. i.e., $Q J_\varphi^T(q) = 0$. Therefore, $J_{\varphi_1}(q) \in \ker(Q)$, and the space \mathfrak{R}^n is decomposed into the two orthogonal subspaces, $\mathfrak{R}^n = \mathfrak{R}(J_\varphi) \oplus \mathfrak{R}(Q)$.

Remark 2. Using a generalization of the implicit function theorem, we can state that Q is well posed $\forall q \in \Omega_q$, where $\Omega_q = \{q | \text{rank}(J(q)) = n, \forall q \in \mathfrak{R}^n\}$ stands for the robot workspace free of singularities. This defines a global decomposition for the 2D case. However, for the 3D case this approach will require an efficient algorithm to compute the independent coordinates on line because the solution of the implicit equation may be not unique. Note, however, that the numerical stability of the decomposition is preserved [25].

4.3 Open Loop Error Equation

Due to the fact that the linear parametrization $Y_r \theta$ depends on $\ddot{q}_r = f(\ddot{x}_r, \ddot{q}_{rf})$, the computation of \ddot{q}_{rf} and \ddot{x}_r gives

$$\ddot{x}_r = \ddot{x}_{vd} - \Psi \Delta \dot{x}_v + \dot{S}_{vd} - \Gamma_{v_1} S_{v\delta} - \Gamma_{v_2} \text{sign}(S_{v\delta}) \quad (28)$$

$$\ddot{q}_{rf} = \Delta \dot{F} - \dot{S}_{dF} + \Gamma_{F_1} S_{F\delta} + \Gamma_{F_2} \text{sign}(S_{F\delta}) \quad (29)$$

which introduces discontinuous terms. To avoid introducing high frequency discontinuous signals, we need to get rid of discontinuous signals in $Y_r \Theta$. To this end, add and subtract $\tanh(\mu_v S_{v\delta})$ and $\tanh(\mu_F S_{F\delta})$ to \ddot{q}_r , assuming that $\mu_F > 0, \mu_v > 0$. Then, \ddot{q}_r becomes

$$\ddot{q}_r = \ddot{q}_{rc} + Q \Gamma_{v_2} z_v - J_\varphi^T(q) \Gamma_{F_2} z_F \quad (30)$$

with $z_v = \tanh(\mu_v S_{v\delta}) - \text{sign}(S_{v\delta})$ and $z_F = \tanh(\mu_F S_{F\delta}) - \text{sign}(S_{F\delta})$, and

$$\ddot{q}_{rc} = Q J_{Rinv} \ddot{x}_{rc} + \dot{Q} J_{Rinv} \dot{x}_{rc} + Q \dot{J}_{Rinv} \dot{x}_{rc} + \Gamma_{F_2} J_\varphi^T(q) \ddot{q}_{rfc} + \Gamma_{F_2} \dot{J}_\varphi^T(q) \dot{q}_{rfc}$$

for

$$\ddot{x}_{rc} = \ddot{x}_{vd} - \Psi \Delta \dot{x}_v + \dot{S}_{vd} - \Gamma_{v_1} S_{v\delta} - \Gamma_{v_2} \tanh(\mu_v S_{v\delta}) \quad (31)$$

$$\ddot{q}_{rfc} = \Delta \dot{F} - \dot{S}_{dF} + \Gamma_{F_1} S_{F\delta} + \Gamma_{F_2} \tanh(\mu_F S_{F\delta}) \quad (32)$$

Therefore, the linear parametrization (6) becomes

$$H(q) \ddot{q}_r + C(q, \dot{q}) \dot{q}_r + g(q) = Y_c \Theta_c + H(Q \Gamma_{v_2} z_v - J_\varphi^T(q) \Gamma_{F_2} z_F) \quad (33)$$

In this formulation, $Y_c = Y_r(q, \dot{q}, \ddot{q}_r, \ddot{q}_{rc})$ is continuous since $(\dot{q}_r, \ddot{q}_{rc}) \in \mathcal{C}^1$, where $Y_c \Theta_c = H(q) \ddot{q}_{rc} + C(q, \dot{q}) \dot{q}_{rc} + g(q)$. Adding and subtracting (33) to (1), we obtain the following open loop error equation

$$H(q) \dot{S}_q = \tau - C(q, \dot{q}) S_q + J_{\varphi+}^T(q) \lambda - Y_c \Theta_c + H(Q \Gamma_{v_2} z_v - J_\varphi^T(q) \Gamma_{F_2} z_F) \quad (34)$$

We are ready to present the main result.

5 Control Design

Assume that (x_v, \dot{x}_v) can be measured by the camera, (q, \dot{q}) can be measured by, respectively, encoders and tachometers, and (λ, F) can be measured by a force sensor. Assume also that the desired image trajectory is free of singularities, i.e., $(x_{vd}, \dot{x}_{vd}) \in \Omega_x$, for $\Omega_x = \{x_v | \text{rank}(J_{Rinv}) = 2, \forall x_v \in \mathbb{R}^2\}$, and $\lambda_d \in C^1$. Then, we have the following theorem.

Theorem 1. *Assume that the initial conditions and the desired trajectories belong to $\Omega_T = [\Omega_q, \Omega_x]$, for $\Omega_q = \{q | \text{rank}(J(q)) = 2, \forall q \in \mathbb{R}^2\}$, and consider the robot dynamics (1)-(2) with the following visual adaptive force-position control law*

$$\begin{aligned} \tau = & -K_d S_q + Y_c \hat{\theta}_b + J_{\varphi+}^T(q) [-\lambda_d + \eta \Delta F] \\ & + \Gamma_{F_2} J_{\varphi+}^T(q) \left[\tanh(\mu_F S_{F\delta}) + \eta \int_{t_0}^t \text{sgn}[S_{F\delta}(\zeta)] d\zeta \right] \end{aligned} \quad (35)$$

$$\dot{\hat{\theta}}_b = -\Gamma Y_c^T S_q \quad (36)$$

where $\hat{\theta}_b$ is the online estimate of the robot parameters, $\Gamma = \Gamma^T \in \mathbb{R}_+^{p \times p}$, $K_d = K_d^T \in \mathbb{R}_+^{n \times n}$, and $\eta > 0$. If K_d is large enough and the errors of initial conditions are small enough, and if

$$\Gamma_{v_2} \geq \left\| \frac{d}{dt} [Q_\theta^\# S_q] \right\|, \quad \Gamma_{F_2} \geq \left\| \frac{d}{dt} [J_\varphi^\# S_q] \right\|$$

where $Q_\theta^\# = R_\alpha(\theta_v) J(q) (Q^T Q)^{-1} Q^T$, and $J_\varphi^\#(q) = (-\Gamma_{F_1} J_\varphi J_\varphi^T(q))^{-1} J_\varphi$, the global exponential convergence of the visual and force tracking errors is guaranteed for any value of the rotational camera angle Θ_v .

Proof. The proof is based on the Lyapunov stability theory along with the variable structure control theory for second order sliding modes. A brief outline of the proof can be stated as follows:

- Part I: Boundedness of the closed loop trajectories. In this part, the passivity from the joint velocity error input to the torque output is established. If the viscous friction is considered, then the dissipativity is established. This implies that the boundedness of the closed loop signals is proved.
- Part II: Second order sliding modes. Once the boundedness of the input signals is proved, the sliding mode regime for the visual and force subspaces needs to be induced. The proper gains are selected in this part.
- Part III: Exponential convergence of the tracking errors. A proper selection of the gains guarantees the sliding mode for each subspace for all time. Then, we prove that each sliding mode induces the exponential convergence of the visual tracking errors and the force tracking errors for all time.

The details of the proof are given in the Appendix. ■

6 Discussions

6.1 Robustness issues

The closed loop system gives rise to two sliding modes. It is well known that the sliding modes are extraordinary robust to parametric uncertainties for certain classes of bounded unmodeled dynamics.

6.2 Well-posed inverse Jacobian

Apparently there can be a problem with $J(q(t))^{-1}$. The visual position exponentially converges to the desired visual position without overshoot, i.e., $x_v(t) \rightarrow x_{vd}(t)$, $x_{vd}(t) \in \Omega_x \implies x_v(t) \in \Omega_x$. However, it does not guarantee that $J(q(t))^{-1}$ is always well posed only because the joint position q converges to the desired joint position q_d with an exponential envelope. The joint position q may experience a short transient and as a consequence $J(q)$

may lose its rank. However, since $q(t)$ converges to $q_d(t)$ locally, it means that $J(q(t)) \rightarrow J(q_d(t))$ within Ω_q . Consequently $J(q(t))^{-1}$ is locally well posed, i.e., $\forall t \text{ rank}[J(q(t))^{-1}] = 2$. In addition, in visual servoing tasks it is customary to design the desired trajectories to be within Ω_x , and therefore within Ω_q , away from singular joint configurations.

6.3 Smooth controller

The continuous function $\tanh(*)$ is used instead of $\text{sign}(*)$ in the control law without jeopardizing the second order sliding mode. Moreover, notice that the $\text{sign}(*)$ is not required to induce a second order sliding mode. This is in contrast to the first order sliding modes theory.

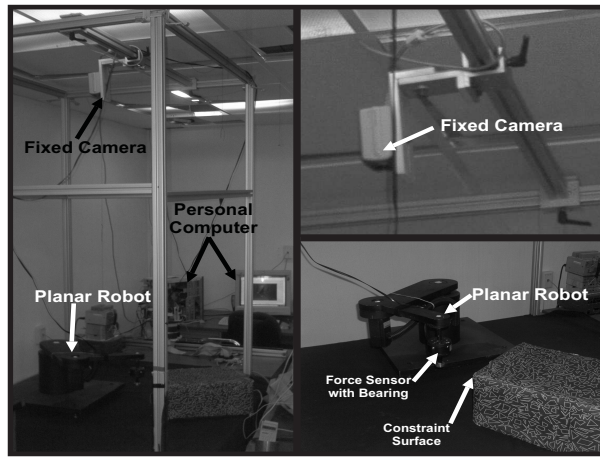


Fig. 2. Experimental setup

6.4 The control structure

The control law features a low computational cost and is easy to implement. The structure of the control law is, basically, similar to that presented in [6], [24] except for the camera information processing part.

7 Experimental System

A planar robot with two degrees of freedom (see Fig. 2) is used in our experiments. The robot and camera parameters are listed in, respectively, Tables 1 and 2. The control feedback gains are listed in Table 3.

7.1 Hardware

Direct-drive Yaskawa AC servomotors SGM-08A314 and SGM-04U3B4L with 2048 pulse encoders are directly coupled to the links of the robot. Digital drives (Yaskawa servopacks SGD-08AS and SGDA-04AS) are integrated into the robot control system. A six-axes force-moment sensor 67M25A-I40-200N12 by JR3 Inc., provided with a DSP Based Interface System for PCI bus, is mounted on the end-effector of the robot. A rigid aluminum probe, with a bearing SKF R8-2Z in its tip, is attached to the end-effector as shown in Fig. 2. The robot task is to move its tool-tip along a specified trajectory over the steel surface while exerting a specified profile of the force normal to the surface. A fixed SONY DFW-VL500 CCD camera is used to capture the position of the robot end effector in the image space (measured in *pixels*). The robot is initialized with a high gain PD control. The inertial frame of the whole system is at the base of the robot, and the contact surface is an XZ plane located at $y = 122$ *pixels*.

7.2 Software

A 2.2 GHz personal computer, running on Debian GNU/Linux 3.1 (kernel 2.4-27) with RTAI patch operating system (rtai 3.1.0-4) is used in the experiments. This PC implements two real-time concurrent processes. The first one communicates with the camera via IEEE1394 protocol and controls the acquisition of the robot end-effector position in the image space at a sampling rate of 30 Hz. The second process computes the torque output for the servopacks and runs at a sampling rate of 1 KHz. The communication between the processes is done by allocating a shared memory. A data acquisition board is connected to the computer. It contains an internal analog quadrature encoder interface, 14 bit analog resolution outputs, and digital I/O ports. The velocity is computed using a dirty Euler numerical differentiation formula filtered with a low pass second order Butterworth filter with a cutoff frequency of 20Hz.

Table 1. Robot Parameters.

Parameter	Mass	Length	Center of Mass	Inertia
Link 1	7.1956 <i>Kg</i>	0.4 <i>m</i>	0.1775 <i>m</i>	0.2779 <i>Kgm²</i>
Link 2	1.8941 <i>Kg</i>	0.3 <i>m</i>	0.0979 <i>m</i>	0.02339 <i>Kgm²</i>

Table 2. Camera Parameters.

Parameter	Value
Rotation angle θ_v	90
Scale factor α	99500 <i>pixel/m</i>
Depth field of view z	1.6 <i>m</i>
Camera offset β	$[-335, -218]^T$ <i>pixel</i>
Focal length ξ	0.08 <i>m</i>

7.3 Control Task

The initial configuration of the robot is shown in the camera image space in Fig. 3.A. Also depicted there are the path of the robot's free motion and the direction of the constrained movement. The control task consists of the following three steps.

1. The end-effector is requested to move until it makes contact with the surface as shown in Fig. 3.B. The free motion time interval is $[0, 3]$ s. Next, within $t \in [3, 5]$ s the end-effector establishes a stable contact with the constraint surface.
2. The tool-tip exerts a desired profile of the force normal to the surface (from 0 to 7.5 N) while moving forward along the X axis from 403 *pixels* to 254 *pixels* (see Fig. 3.C). This is done in the time span $t \in [5, 10]$ s
3. In the time interval $t \in [10, 15]$ s the exerted force is incremented from 7.5 to 15 N, while moving the tool-tip (see Fig. 3.C) backward along the X axis from 254 *pixels* to 403 *pixels*.

The desired position and force are both designed with

$$\Phi(t) = P(t) [\mathbf{X}_f - \mathbf{X}_i] + \mathbf{X}_i, \quad (37)$$

where $P(t)$ is a fifth order polynomial that satisfy $P(t_i) = 0, P(t_f) = 1$ and $\dot{P}(t_i) = \dot{P}(t_f) = 0$. The subscript i and f denote the initial and the final moments, respectively. At the first stage of the control task (free motion), the control law (35)-(36) is used with $J_\varphi^T(q) = 0$ and $Q = I$. The stability of this free motion control scheme is proved in [26].

7.4 Experimental Results

The performance of the simultaneous force and position tracking is illustrated in Fig. 4, 5, 6, and 7. Fig. 10 gives an image of the visual tracking of the robot's end effector. The motion of the robot's end-effector in the image space is shown in Fig. 5 and 6. Note that the image coordinated system is rotated by θ_v degrees (in this case 90°). The maximum tracking error is 1 *pixel* (near to 0.20mm). The tracking performance can be improved by using a sub-pixel resolution.

Table 3. Feedback Gains.

Gain	Value	Gain	Value	Gain	Value	Gain	Value
K_d	$\begin{bmatrix} 14 & 0 \\ 0 & 1.8 \end{bmatrix}$	κ_v	20	$\Gamma_{v(1,2)}$	$\begin{bmatrix} 8 & 0 \\ 0 & 8 \end{bmatrix}$	Γ	1
Ψ	$\begin{bmatrix} 5 & 0 \\ 0 & 5 \end{bmatrix}$	κ_F	20	$\Gamma_{F(1,2)}$	3	η	2.8

Fig. 8 shows the joint torques. As can be seen from Fig. 8, the control output is not saturated. The torque noise in the free motion segment is due to the fact that the control gains are tuned for the position-force control task. These gains are high during the free motion time, and this causes the high response observed in Fig. 8. Fig. 9 depicts the exponential envelope of the Cartesian tracking errors. Fig. 4 shows the exerted force profile. As can be seen, from $t = 0s$ to $t = 3s$ the robot's end effector is in free motion (the contact force is near $0N$) until it makes contact with the surface (an overshoot in the contact force is presented due to contact transition). The end-effector remains in that state 2 more seconds. The applied force is smoothly increased from $0N$ to $7.5N$ while the end-effector moves forward along the X axis in the time interval $[5\ 10]s$. Then, in the time interval $[10\ 15]s$ the applied force is increased from $7.5N$ to $15N$ while the end-effector moves backward. The seemingly high frequency in the force response can be explained by the precision of the sensors. The movement task requires a very precise control, but the sensor resolution is limited to $1\ pixel$ and the JR3 force sensor noise is $\pm 2N^7$.

⁷ Better plots can be obtained by simply reducing the desired visual velocity or by increasing $\lambda_d(t)$.

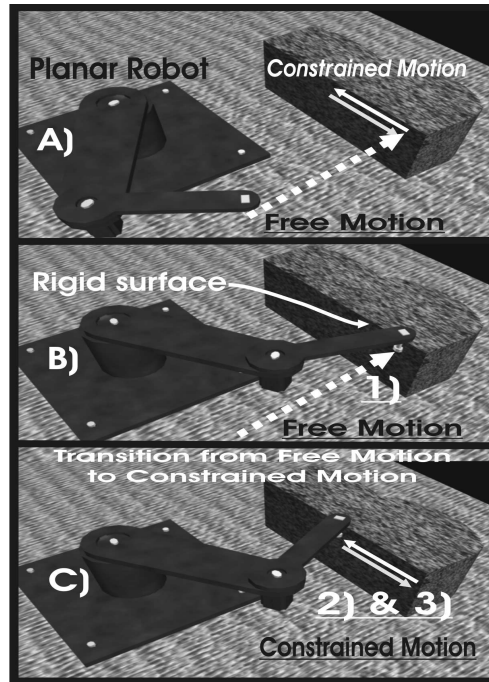


Fig. 3. Experimental phases

8 Conclusions

A novel scheme for the adaptive image-based visual servoing of constrained robots was proposed in this chapter. The new scheme is based on the Visual Orthogonalization Principle (VOP). The main feature of the control scheme is the ability to fuse the *image coordinates* and the *integral of contact forces*. The scheme guarantees a global *exponential convergence* for the image-based position-velocity and the contact forces even when the robot parameters are considered unknown. The experimental results confirm the stability of the control scheme. The novel control scheme can improved to deal with the uncertainties in the description of the constraint surface, the robot Jacobian, and the friction forces. The scheme can be used in a number of control tasks employing the dynamic visual servoing. These task include the cooperative control of multiple robot arms and multi-fingered robotic hands. It can be also used in the control of biped walking machines⁸.

Appendix: Proof of Theorem 1

The closed loop dynamics (35)~(36) and (34) yields

$$H(q) \dot{S}_q = -\{K_d + C(q, \dot{q})\} S_q - Y_c \Delta \theta_b + J_{\varphi+}^T(q) [\Delta \lambda + \Gamma_{F_2} \tanh(\mu_F S_{F\delta})] + \eta J_{\varphi+}^T(q) \left[\Delta F + \Gamma_{F_2} \int_{t_0}^t \text{sgn}(S_{F\delta}(\zeta)) d\zeta \right] \quad (38)$$

$$\Delta \dot{\theta}_b = \Gamma Y_c^T S_q \quad (39)$$

where $\Delta \theta_b = \theta_b - \hat{\theta}_b$. The proof is organized in three parts.

Part I. Boundedness of the closed loop trajectories. Consider the time derivative of the following *Lyapunov* candidate function

⁸ The examples can be found in www.manyrob.cinvestav.mx.

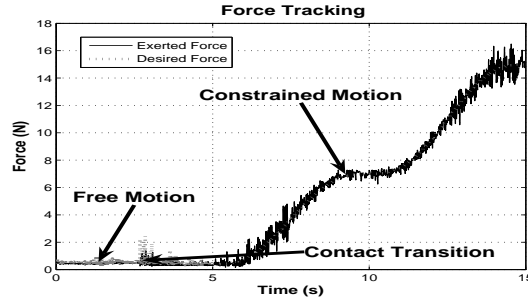


Fig. 4. Force Tracking

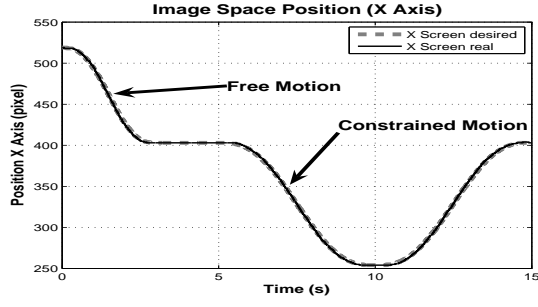


Fig. 5. End effector x position in image space (pixels).

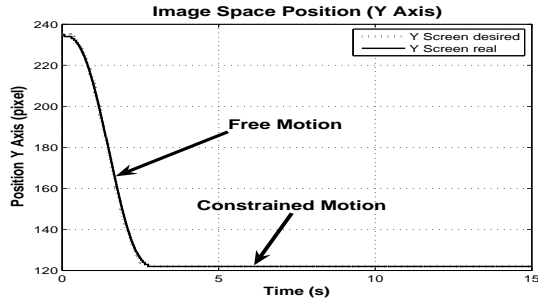


Fig. 6. End effector position in image space (pixels).

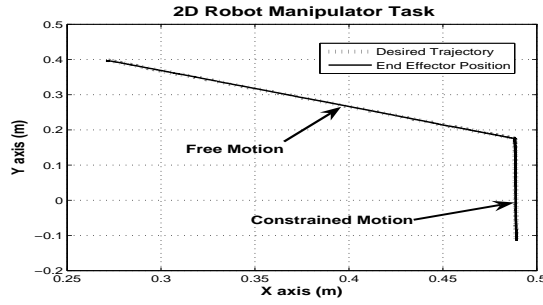


Fig. 7. Cartesian robot task in robot space (m).

$$V = \frac{1}{2} [S_q^T H(q) S_q + \Gamma_{F_2} S_{vF}^T S_{vF} + \Delta \theta_b^T \Gamma^{-1} \Delta \theta_b] \quad (40)$$

Along the solutions of (38)-(39) we have

$$\dot{V} \leq -K_d \|\hat{S}_q\|_2^2 - \Gamma_{F_2} \|S_{vF}\| + \|\hat{S}_q\| \psi \quad (41)$$

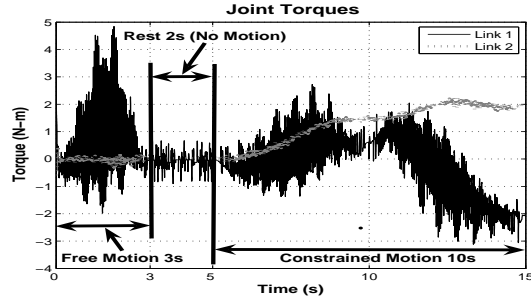


Fig. 8. Input torques.

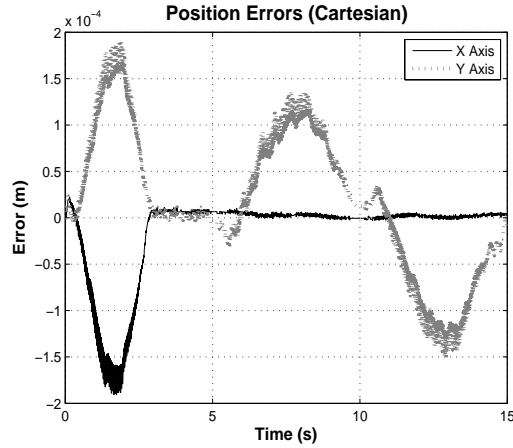


Fig. 9. Cartesian tracking error with exponential envelope.

where $S_q^T \left(\frac{1}{2} \dot{H}(q) - C(q, \dot{q}) \right) S_q = 0$ and ψ is a functional depending on the state and error manifolds [27]. If K_d and Γ_{F_2} are large enough and the errors in initial conditions are small enough, we conclude the semi-negative definiteness of (41) outside of the hyperball $\varepsilon_0 = \{S_q | \dot{V} \leq 0\}$ centered at the origin. Therefore, the following properties of the state of the closed loop system take place

$$(S_q, S_{vF}) \in \mathcal{L}_\infty \rightarrow (\|S_{vv}\|, \|S_{vF}\|) \in \mathcal{L}_\infty \quad (42)$$

Then, $\left(S_{v\delta}, \int_{t_0}^t \text{sign}(S_{v\delta}(\zeta)) d\zeta \right) \in \mathcal{L}_\infty$ and since the desired trajectories are differentiable functions and the feedback gains are bounded, we have $(\dot{q}_r, \ddot{q}_r) \in \mathcal{L}_\infty$. The right hand side of (38) shows that there exists $\varepsilon_1 > 0$ such that $\|\dot{S}_q\| \leq \varepsilon_1$. Since $S_q \in \mathcal{L}_2$ and J_{Rinv} and Q are bounded, then $QJ_{Rinv}S_{vv}$ is bounded. Since $\varphi(q)$ is smooth and lies in the reachable robot space and

$S_{vF} \rightarrow 0$, then $J_\varphi^T(q) \Gamma_{F_2} S_{vF} \rightarrow 0$. Now, taking into account that \dot{S}_q is bounded, then $\frac{d}{dt}(J_{Rinv} Q S_{vv})$ and $\frac{d}{dt}(J_\varphi^T(q) \Gamma_{F_2} S_{vF})$ are bounded (this is possible because $J_\varphi^T(q)$ is bounded and so is \dot{Q}). All these conclusions prove that there exist constants $\varepsilon_2 > 0$ and $\varepsilon_3 > 0$ such that

$$\left| \dot{S}_{vv} \right| < \varepsilon_2, \left| \dot{S}_{vF} \right| < \varepsilon_3$$

So far, the analysis shows only the stability of all the closed-loop signals. Now we prove the appearance of the sliding modes. To this end, we have to prove that for the properly selected feedback gains Γ_{v_2} and Γ_{F_2} the trajectories of the visual position and force converge to zero. This can be done if we can prove that the sliding modes are established in the visual subspace Q and in the force subspace $J_\varphi^T(q)$.

Part II: Second order sliding modes.

Part II.a: Sliding modes for the velocity subspace. From (21) we obtain

$$(Q^T Q)^{-1} Q^T S_q \equiv J_{Rinv} S_{vv} \quad (43)$$

By multiplying (43) by $\alpha h(z) R(\theta) J(q)$ and substituting it into (22), we have

$$Q_\theta^\# S_q = S_{v\delta} + \Gamma_{v_1} \int_{t_0}^t S_{v\delta}(\zeta) d\zeta + \Gamma_{v_2} \int_{t_0}^t \text{sign}(S_{v\delta}(\zeta)) d\zeta \quad (44)$$

Taking the time derivative of (44), and multiplying it by $S_{v\delta}^T$, we have

$$\begin{aligned} S_{v\delta}^T \dot{S}_{v\delta} &= -\gamma_{v_2} S_{v\delta}^T \text{sign}(S_{v\delta}) - \Gamma_{v_1} S_{v\delta}^T S_{v\delta} + S_{v\delta}^T \frac{d}{dt} [Q_\theta^\# S_q] \\ &\leq -\mu_v |S_{v\delta}| - \Gamma_{v_1} \|S_{v\delta}\|^2 \end{aligned} \quad (45)$$

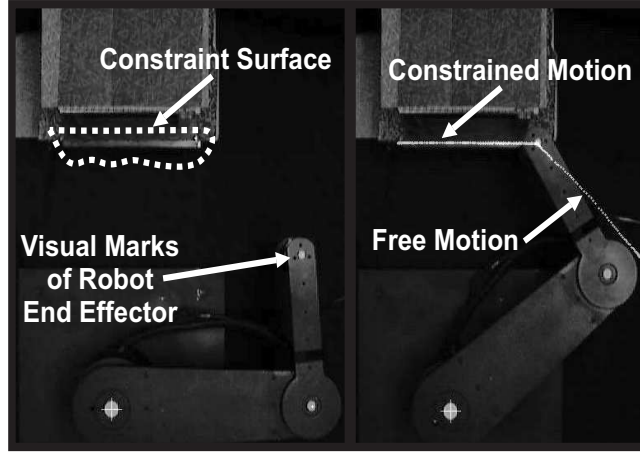


Fig. 10. Camera view point.

where $\mu_v = \Gamma_{v_2} - \varepsilon_4$, and $\varepsilon_4 \geq \left| \frac{d}{dt} [Q_\theta^\# S_q] \right|$. Thus, we obtain the sliding condition $\Gamma_{v_2} > \varepsilon_4$. Therefore, $\mu_v > 0$ in (45) guarantees a sliding mode at $S_{v\delta} = 0$ when $t_v = \frac{|S_{v\delta}(t_0)|}{\mu_v}$. However, notice that for any initial condition $S_{v\delta}(t_0) = 0$ we have $t_v = 0$, which implies that the sliding mode at $S_{v\delta}(t) = 0$ is guaranteed for all time.

Part II.b: Sliding modes for the force subspace. In much the same way as has been done in Part II.a, we process equation (21) to obtain

$$J_\varphi^\#(q) S_q = S_{F\delta} + \Gamma_{F_1} \int_{t_0}^t S_{F\delta}(\zeta) d\zeta + \Gamma_{F_2} \int_{t_0}^t \text{sign}(S_{F\delta}(\zeta)) d\zeta \quad (46)$$

Taking the time derivative of (46) and multiplying it by $S_{F\delta}^T$, (46), we have

$$S_{F\delta}^T \dot{S}_{F\delta} = -\Gamma_{F_2} |S_{F\delta}| - \Gamma_{F_1} S_{F\delta}^T S_{F\delta} + S_{F\delta}^T \frac{d}{dt} (J_\varphi^\#(q) S_q) \quad (47)$$

$$\leq -\Gamma_{F_2} |S_{F\delta}| - \Gamma_{F_1} \|S_{F\delta}\|^2 + |S_{F\delta}| \frac{d}{dt} (J_\varphi^\#(q) S_q) \quad (48)$$

$$\leq -\mu_F |S_{F\delta}| - \Gamma_{F_1} \|S_{F\delta}\|^2 \quad (49)$$

where $\mu_F = \Gamma_{F_2} - \varepsilon_5$, and $\varepsilon_5 \geq \frac{d}{dt} [J_\varphi^\#(q) S_q]$. If $\Gamma_{F_2} > \varepsilon_5$, then a sliding mode at $S_{F\delta}(t) = 0$ is induced at $t_f \leq \frac{|S_{F\delta}(t_0)|}{\mu_F}$, but $S_{F\delta}(t_0) = 0$ and thus $S_{F\delta}(t_0) = 0$ is guaranteed for all time.

Part III: Exponential convergence of tracking errors.

Part III.a: Visual tracking errors. Since a sliding mode exists for all time at $S_{v\delta}(t) = 0$, then we have

$$S_v = S_{vd} \quad \forall t \rightarrow \Delta \dot{x}_v = -\Psi \Delta x_v + S_v(t_0) e^{-\kappa_v t}$$

This implies that the visual tracking errors globally and exponentially converge to zero and $x_v \rightarrow x_{vd}$, $\dot{x}_v \rightarrow \dot{x}_{vd}$. Therefore, in the image space the end-effector reaches the desired position x_{vd} with the desired velocity \dot{x}_{vd} .

Part III.b: Force tracking errors. Since a sliding mode at $S_{F\delta}(t) = 0$ is induced for all time, we have $\Delta F = \Delta F(t_0) e^{-\kappa_F t}$. From this we obtain $\Delta \dot{F} \equiv \Delta \lambda = -\kappa_F \Delta F(t_0) e^{-\kappa_F t}$, showing the global convergence of the force tracking errors. Thus λ reaches λ_d exponentially fast. **QED.**

References

1. Whitney D (1997) Force feedback control of manipulator fine motions. ASME Journal of Dynamic Systems, Measurement and Control 99:91-97
2. Whitney D (1985) Historical perspective and state of the art in robot force control. In: Proc. IEEE Int. Conf. on Robotics and Automation 262-268
3. De Schutter J, Bruyninckx H, Zhu WH, Spong M (1997) Force control: A bird's eye view. In: Proc. IEEE CSS/RAS Int. Workshop on Control Problems in Robotics and Automation: Future Directions

4. Arimoto S (1996) Control Theory of Non-linear Mechanical Systems: A Passivity-based and Circuit-theoretic Approach. Oxford Engineering Science Series, Oxford University Press
5. McClamroch H, Wang D (1988) Feedback stabilization and tracking of constrained robots. *IEEE Transactions on Automatic Control* 33(5):419–426
6. Arimoto S, Liu YH, Parra-Vega V (1992) Design of model-based adaptive controllers for robot manipulators under geometric constraints. In: Proc. The Japan-USA Symposium on Flexible Automation, USA 615–621
7. Liu YH, Arimoto S, Parra-Vega V, Kitagaki K (1997) Decentralized adaptive control of multiple manipulators in co-operation. *International Journal of Control* 67(5):649–673
8. Parra-Vega V, Rodriguez-Angeles A, Arimoto S, Hirzinger G (2001) High precision constrained grasping with cooperative adaptive hand control. *Journal of Intelligent and Robotic Systems* 32(3):235–254
9. Hutchinson S, Hager G, Corke P (1996) A tutorial on visual servo control. *IEEE Transactions on Robotics and Automation* 12(5):651–670
10. Weiss L, Sanderson A, Neuman C (1987) Dynamic sensor based control of robots with visual feedback. *IEEE Journal of Robotics and Automation* 3(5):404–417
11. Papanikolopoulos N, Khosla P, Kanade T (1993) Visual tracking of a moving target by a camera mounted on a robot: A combination of control and vision. *IEEE Journal of Robotics and Automation* 9:14–35
12. Castano A, Hutchinson S (1994) Visual compliance: Task directed visual servo control. *IEEE Transactions on Robotics and Automation* 10(3):334–342
13. Bishop B, Spong M (1997) Adaptive calibration and control of 2D monocular visual servo system. In: Proc. IFAC Symposium on Robot Control, Nantes, France 525–530.
14. Miyazaki F, Masutani Y (1990), Robustness on sensory feedback control based on imperfect jacobian, In: Robotics Research: The Fifth Int Symp, Miura H, Arimoto S (eds.), MIT, Cambridge, MA, 201–208.
15. Kelly R, Marquez A (1995) Fixed-eye direct visual feedback control of planar robots. *Journal of System Engineering* 4(5):239–248
16. Kelly R (1996) Robust asymptotically stable visual servoing of planar robots. *IEEE Transactions on Robotics and Automation* 12(5):759–766
17. Zergeroglu E, Dawson D, de Queiroz M, Setlur P (2003) Robust visual-servo control of robot manipulators in the presence of uncertainty. *Journal of Robotic Systems* 20(2):93–106
18. Dean-León E, Parra-Vega V, Espinosa-Romero A, Fierro J (2004) Dynamical image-based PID uncalibrated visual servoing with fixed camera for tracking of planar robots with a heuristical predictor. In: Proc. 2nd IEEE Int. Conf. on Industrial Informatics 339–345
19. Shen Y, Sun D, Liu YH, Li KJ (2003) Asymptotic trajectory tracking of manipulators using uncalibrated visual feedback. *IEEE/ASME Transactions on Mechatronics* 8(1):87–9
20. Xiao D (2000) Sensor-hybrid position/force control of a robot manipulator in an uncalibrated environment. *IEEE Transactions on Control System Technology* 8(4):635–645
21. Nelson B, Khosla P (1996) Force and vision resolvability for assimilating disparate sensory feedback. *IEEE Transactions on Robotics and Automation* 12(5):714–731

22. Baeten J, De Schutter J (2001) Combined vision/force control at corners in planar robotic contour following. In: Proc. IEEE/ASME Int. Conf. on Advanced Intelligent Mechatronics 810–815
23. Hosoda K, Igarashi K, Asada M (1998) Adaptive hybrid control for visual and force servoing in an unknown environment. IEEE Robotics and Automation Magazine 5:39–43
24. Parra-Vega V, Arimoto S, Liu YH, Naniwa T (1994) Model-based adaptive hybrid control of robot manipulators under holonomic constraints. In: Proc. IFAC Symposium on Robot Control 475–480
25. Blajer W, Schiehlen W, Schirm W (1994) A projection criterion to the coordinate partitioning method for multi body dynamics. Archive of Applied Mechanics 84:86–98
26. García L, Dean-León E, Parra-Vega V, Espinosa-Romero A, Fierro J (2005) Experimental results of image-based adaptive visual servoing of 2D robots under jacobian and dynamic friction uncertainties. In: Proc. Int. Symposium on Computational Intelligence in Robotics and Automation
27. Parra-Vega V, Arimoto S, Liu YH, Hirzinger G, Akella P (2003) Dynamic sliding PID control for tracking of robot manipulators: theory and experiments. IEEE Transactions on Robotics and Automation 19:967–976